Applied Catalysis B: Environmental 224 (2018) 17–26

Contents lists available at ScienceDirect

Applied Catalysis B: Environmental

journal homepage: www.elsevier.com/locate/apcatb

Research paper

Synergistic effect based Ni_xCo_{1-x} architected $Zn_{0.75}Cd_{0.25}S$ nanocrystals: An ultrahigh and stable photocatalysts for hydrogen evolution from water splitting

Xinzheng Yue[a], Shasha Yi[b], Runwei Wang[a], Zongtao Zhang[a,*], Shilun Qiu[a]

[a] State Key Laboratory of Inorganic Synthesis and Preparative Chemistry, College of Chemistry, Jilin University, Changchun, 130012, China

[b] Key Laboratory of Automobile Materials, Ministry of Education, Department of Materials Science and Engineering, Jilin University, Changchun, 130022, China

ARTICLE INFO

Keywords:
Photocatalytic
H_2
$Zn_{0.75}Cd_{0.25}S$
Ni_xCo_{1-x}
Hybrid

ABSTRACT

Construction of functional photocatalysts with ultrahigh photocatalytic hydrogen evolution using solar energy is still a serious challenge for scientific researchers. Here, recently, a facile chemical reduction method is developed to synthesize $Ni_xCo_{1-x}/Zn_{0.75}Cd_{0.25}S$ nanohybrid photocatalysts, a kind of promising smart material with optimizing H_2 evolution rate being 0.21 mol h^{-1} g^{-1} under simulated solar light irradiation with an apparent quantum efficiency (AQE) of 13.3% at 365 nm, an ultrahigh H_2 evolution rate among almost all the semiconductor-based photocatalysts. More importantly, the $Ni_xCo_{1-x}/Zn_{0.75}Cd_{0.25}S$ photocatalyst shows a sufficient stability property for > 20 h. The pronounced synergistic effect between non-noble-metals of Ni and Co boosts the transfer and separation of photo-generated electron-hole pairs, and a synergistic catalytic mechanism has been proposed and studied in detail.

1. Introduction

It is an indisputable fact that direct evolution of hydrogen (H_2) from water splitting through solar energy can be a forefront and sustainable energy conversion technology to relieve environment pollution and energy security [1–3]. Photocatalytic water splitting to produce H_2 affords the energy needs of the society on a large scale, and extensive research efforts have been done directly for improving its performance on numerous active photocatalysts, such as, sulfide, oxide, nitride, oxynitride, and perovskite, etc [1,4–10]. Now the critical challenge is to design the satisfactory photocatalysts with high-efficiency, low-cost, environmentally friendly, and sustainability to drive H_2 evolution from water splitting by solar energy. Nevertheless, semiconductor-based materials usually suffer the high recombination incident of electrons and holes and make their low-energy conversion efficiency, which is a vital factor in determining their performance. To address this issue, platinum (Pt) is widely used loading as the cocatalyst to draw the electrons out to the surface, thus enhancing the lifetimes of photo-generated charge carriers [2]. However, the high cost of Pt confines its use in industrial scale water splitting for H_2 evolution strategy. Hence, it is highly desirable to choice a suitable photocatalyst together with the natural abundance cocatalyst that constructing an efficient material for H_2 evolution.

Recently, the research for metal sulfide/selenide based solid solutions have been intensively studied and impressive achievements in artificial photocatalysis have been demonstrated for their suitable conduction band (CB) potential for the H^+ reduction reaction and the well-matched absorption spectrum for solar energy [11–14]. Especially for $Zn_xCd_{1-x}S$, it shows the capability of high visible light induced photocatalytic H_2 evolution activity and photo-stability than that of CdS [13]. Some alternatives based on earth abundant elements have been emerged and proven to be effective cocatalysts for water splitting on $Zn_xCd_{1-x}S$, such as, MoO_2, MoS_2, reduced graphene oxide (RGO), etc [15–17]. Even so, the performance of this type of catalyst is still too low to satisfy the needs of social development.

Elements metal nanoparticles (NPs) of Ni or Co show the similar characteristics of noble Pt [18,19], and their alloy may be envisaged to use as the electron capture agent for $Zn_xCd_{1-x}S$, widening the distance between photo-generated electrons and holes in space, and thus leaving much more electrons to participate photocatalytic reduction reactions. Previous reports have reported that bimetal alloys can be used in various fields, such as, Pt-based transition metal alloys with high oxygen reduction reaction activity [20], BiAg alloy with outstanding photoelectrochemical property [21], NiMo hollow nanorod arrays with superior electrocatalytic for overall water splitting [22], and PtCo alloy NPs decorated $g\text{-}C_3N_4$ with excellent photocatalytic H_2 evolution from

* Corresponding author.
E-mail address: zzhang@jlu.edu.cn (Z. Zhang).

http://dx.doi.org/10.1016/j.apcatb.2017.10.010
Received 30 June 2017; Received in revised form 26 September 2017; Accepted 6 October 2017
Available online 08 October 2017

water splitting [23]. Yet, as far as we know, no research on two earth abundant elements of NiCo has been reported in photocatalytic H_2 evolution reaction.

In this article, for the first time we synthesize an effective hybrid nanophotocatalyst by a facial chemical reduction method for the rational growth of Ni_xCo_{1-x} NPs on $Zn_{0.75}Cd_{0.25}S$ by adjusting components. The resultant $Ni_{0.8}Co_{0.2}/Zn_{0.75}Cd_{0.25}S$ shows super high solar light induced photocatalytic H_2 evolution activity with its rate of 211417 μmol h^{-1} g^{-1}, which is much higher than that of the optimized $Pt/Zn_{0.75}Cd_{0.25}S$ and corresponding to the apparent quantum efficiency (AQE) of 13.3%. Moreover, long time catalytic tests show that the nanocomposite still keep high active after five consecutive operations of 20 h. In this hybrid, Ni_xCo_{1-x} NPs serve as the electron collector, transporter and reduction active site for H_2 evolution. The photocatalytic mechanism based on notable synergistic effect of Ni and Co is also discussed in detail. This work will provide a new insight into the design and fabrication of such nanohybrid photocatalysts with ultrahigh photocatalytic H_2 evolution activity, and promote this photocatalytic research into a new step.

2. Experimental sections

2.1. Chemicals

Zinc acetate dehydrate ($Zn(CH_3COO)_2{\cdot}2H_2O$), cadmium acetate dehydrate ($Cd(CH_3COO)_2{\cdot}2H_2O$), chloroplatinic acid hexahydrate ($H_2PtCl_6{\cdot}6H_2O$), sodium borohydride ($NaBH_4$), and sodium sulfide nonahydrate ($Na_2S{\cdot}9H_2O$) were purchased from Sinopharm Chemical Reagent Co., Ltd. Nickel nitrate hexahydrate ($Ni(NO_3)_2{\cdot}6H_2O$), ethylene diamine tetraacetic acid (EDTA), cobalt nitrate hexahydrate ($Co(NO_3)_2{\cdot}6H_2O$), sodium sulfite anhydrous (Na_2SO_3), ethanol, and triethanolamine (TEOA) were bought from Beijing Chemical Works. Commercial 5 wt% Nafion117 solution was purchased from DuPont. The chemicals were used without any further purification and the deionized water (18.2 MΩ·cm resistivity) used throughout all experiments was obtained by reverse osmosis followed by ion-exchange and filtration.

2.2. Synthesis of $Zn_{0.75}Cd_{0.25}S$ solid solution

In a typical experiment, 7.5 mmol of $Zn(CH_3COO)_2{\cdot}2H_2O$ and 2.5 mmol of $Cd(CH_3COO)_2{\cdot}2H_2O$ were initially added into 70 mL of deionized water to form a transparent solution. Subsequently, certain amounts of $Na_2S{\cdot}9H_2O$ aqueous solution (1 M) was added dropwise into the above solution under stirring, and the mixture was stirred for 3 h. Then, the resulting solution was transferred into a 100 mL Teflon-lined stainless steel autoclave and heated at 180 °C for 12 h. Afterward the precipitates were washed several times with deionized water and ethanol, and then dried at 60 °C overnight. The ICP results showed that the obtained species with its Cd/Zn stoichiometry ratio is nearly 3:1 (Table 1), which is in good agreement with the adding ratio. Then, the obtained $Zn_xCd_{1-x}S$ solid solution is $Zn_{0.75}Cd_{0.25}S$, and labeled as ZCS.

2.3. Synthesis of Ni/ZCS, Co/ZCS, and Ni_xCo_{1-x}/ZCS nanostructures

Typically, 0.25 g of ZCS was dispersed into 15 mL of deionized water with first ultrasonicated for 30 min, then 5 mL of $Ni(NO_3)_2{\cdot}6H_2O$ (4.6 mM) solution was pouring into under stirring. After 10 min, a specified volume of $NaBH_4$ solution (2 mL, 0.6 M) was quickly added to the above liquid, and the mixture was stirred for 1 h. Finally, the obtained products were washed and dried to get 1% Ni/ZCS (the molar ratio of Ni to ZCS was 1%) and labeled as Ni/ZCS. Similarly, Co/ZCS was obtained only by using $Ni(NO_3)_2{\cdot}6H_2O$ be replaced by $Co(NO_3)_2{\cdot}6H_2O$. With the same method above, Ni_xCo_{1-x}/ZCS photocatalysts (the molar ratio of Ni:Co of 1:1, 3:2, and 4:1) were prepared by changing the different volumes of $Ni(NO_3)_2{\cdot}6H_2O$ (4.6 mM) and $Co(NO_3)_2{\cdot}6H_2O$ (4.6 mM) solution, and their corresponding volumes were (2.5 mL, 2.5 mL), (3 mL, 2 mL) and (4 mL, 1 mL), respectively, which labeled as $Ni_{0.5}Co_{0.5}$/ZCS, $Ni_{0.6}Co_{0.4}$/ZCS, and $Ni_{0.8}Co_{0.2}$/ZCS. Note that, keeping the molar ratio of (Ni + Co) to ZCS as a constant of 1%. In addition, the ICP results once again confirm that the target photocatalysts were successfully obtained (Table 1).

Table 1
The concentrations of each element in the solution of ZCS and $Ni_{0.8}Co_{0.2}$/ZCS.

Concentration Samples	mmol L^{-1}				
	Zn	Cd	S	Ni	Co
ZCS	0.347	0.111	0.321	0	0
$Ni_{0.8}Co_{0.2}$/ZCS	0.331	0.104	0.324	0.003	0.0008

2.4. Synthesis of Ni, Co, and NiCo metals

For comparison, Ni, Co, and NiCo metals were synthesized as the same method of Section of 2.3 for Ni/ZCS, Co/ZCS, and NiCo/ZCS without adding ZCS.

2.5. Synthesis of 1% Pt/ZCS nanostructures

For comparison, 1% Pt/ZCS (the molar ratio of Pt to ZCS was 1%) was also prepared as the same method of Section of 2.3, using H_2PtCl_6 as the Pt source.

2.6. Characterizations

The crystalline structure of the as-prepared sample was characterized by powder X-ray diffraction (XRD) with a Rigaku D/Max-2550 diffractometer using Cu Kα radiation (λ = 1.54056 Å) at 50 kV and 200 mA in the 2θ range of 20 − 80° at a scanning rate of 10° min^{-1}. X-ray photoelectron spectroscopy (XPS) measurements were performed on a Thermo VG Scientific ESCALAB 250 spectrometer using monochromatized Al Kα excitation. The optical absorption spectra of the samples were measured on a UV–vis-NIR spectrophotometer (Shimadzu UV-3600) detecting absorption over the range of 300–800 nm. The morphologies of the samples together with its Energy-dispersive X-ray (EDX) spectroscopy were examined by scanning electron microscopy (SEM) using a JSM-6700F field emission scanning electron microscope. The transmission electron microscopy (TEM) and the high-resolution transmission electron microscopy (HRTEM) images were conducted on a Tecnai G2 S-Twin F20 TEM microscope (FEI Company). The element mappings were applied on a HITACHI SU-8020 transmission electron microscopy. Photoluminescence (PL) spectra with an excitation wavelength of 325 nm were measured on a FLUOROMAX-4. The ICP data was acquired on a PerkinElmer OPTIMA 3300DV ICP spectrometer.

The lock-in-based surface photovoltage (SPV) spectroscopic measurement system consisted of a source of monochromatic light, a sample cell, a computer, and a lock-in amplifier (SR830-D SP) with a light chopper (SR540). The monochromatic light was provided by a 500 W xenon lamp (CHF-XM–500 W, Global Xenon Lamp Power) together with a grating monochromator (Omni-5007, Zolix). A low chopping frequency of 24 Hz was used. The samples were studied without further treatment during the SPV measurements, and the photovoltaic cell was a structure of fluorine-doped tin oxide (FTO)-mica-sample-FTO. The system was calibrated by a DSI200 UV enhanced silicon detector to eliminate the possible phase shift which was not correlated to the SPV response, so that any phase retardation reflected the kinetics of SPV response. The work function measurement was carried out on a Kelvin Probe instrument (SKP 5050, KP Technology Ltd, Scotland, UK).

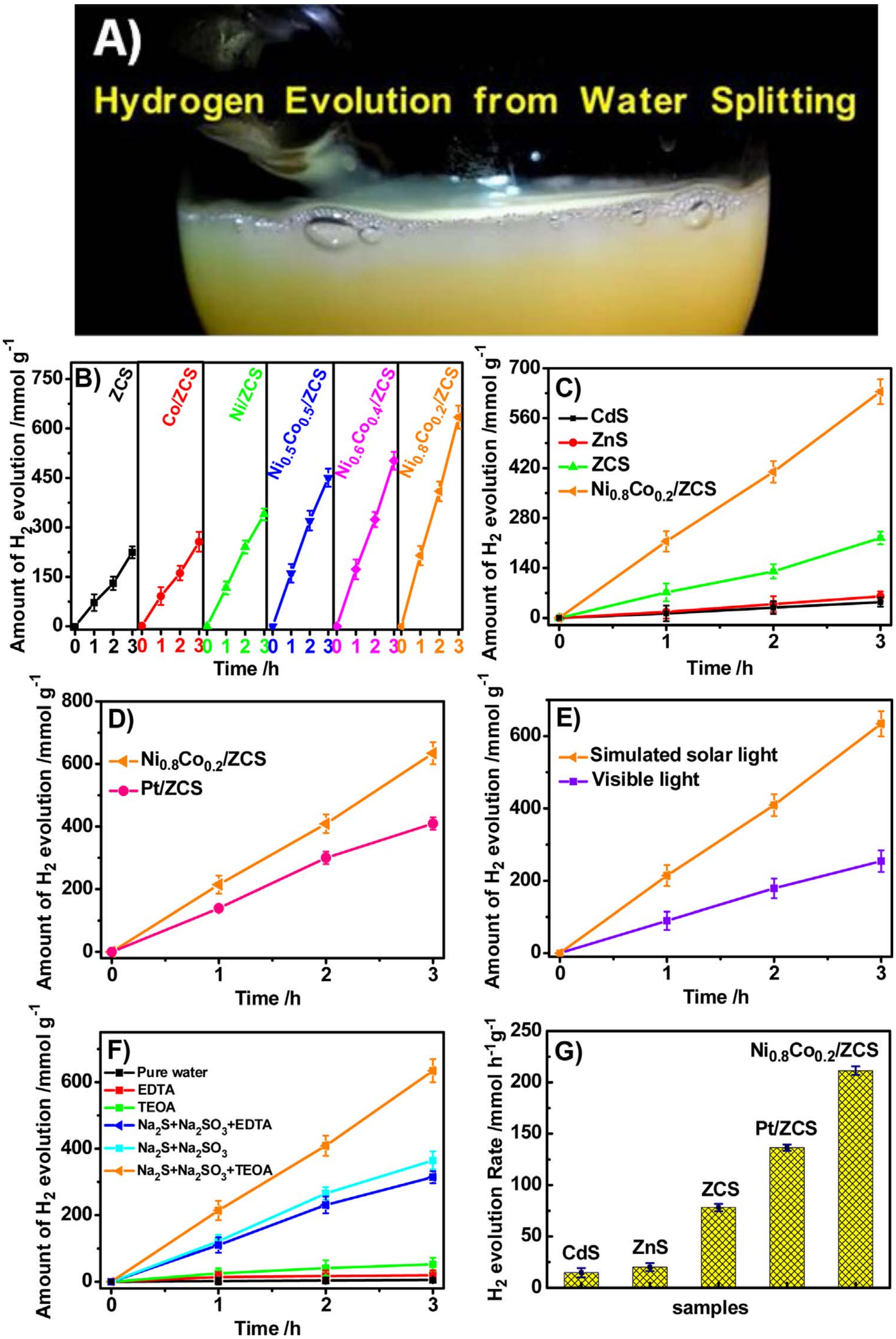

Fig. 1. A) A phtograph showing evolution of H_2 bubbles on the $Ni_{0.8}Co_{0.2}$/ZCS photocatalyst. Time courses of H_2 evolution over B) ZCS and Ni_xCo_{1-x}/ZCS (x = 0, 0.5, 0.6, 0.8 and 1), C) CdS, ZnS, ZCS, and $Ni_{0.8}Co_{0.2}$/ZCS, and D) $Ni_{0.8}Co_{0.2}$/ZCS and 1% Pt/ZCS in aqueous solutions of 0.35 M Na_2S/0.25 M Na_2SO_3 + 5 mL TEOA under simulated solar light irradiation. E) Time courses of H_2 evolution over $Ni_{0.8}Co_{0.2}$/ZCS under both of simulated solar and visible light (λ > 420 nm) irradiation in aqueous solutions of 0.35 M Na_2S/0.25 M Na_2SO_3 + 5 mL TEOA. F) Time courses of H_2 evolution over $Ni_{0.8}Co_{0.2}$/ZCS in different of sacrificial reagent solutions under simulated solar light irradiation. G) Comparison of photocatalytic H_2 evolution rate over CdS, ZnS, ZCS, Pt/ZCS, and $Ni_{0.8}Co_{0.2}$/ZCS in aqueous solutions of 0.35 M Na_2S/0.25 M Na_2SO_3 + 5 mL TEOA under simulated solar light irradiation.

2.7. Photocatalytic H_2 evolution from water splitting

According to experimental explore requirements, the photocatalytic H_2 evolution experiments were performed under specific conditions, 50 mg of photocatalyst suspended in a 100 mL of pure H_2O; 95 mL of H_2O + 5 mL of TEOA; 100 mL of H_2O + 1 g of EDTA; 100 mL of 0.35 M Na_2S/0.25 M Na_2SO_3; 100 mL of 0.35 M Na_2S/0.25 M Na_2SO_3 + 1 g of EDTA; 95 mL of 0.35 M Na_2S/0.25 M Na_2SO_3 + 5 mL of TEOA aqueous solution, respectively, in a Pyrex glass reaction cell at ambient temperature and atmospheric pressure. A 300 W Xe lamp with cooling water (stabilize the temperature at 277 K) was served as the light source to trigger the photocatalytic reaction. Before irradiation, the system was pumped to vacuum to remove the air inside and to ensure that the reaction system is under anaerobic conditions. A 4.23 mL of gas was intermittently sampled and H_2 was analyzed using an online gas chromatograph (GC-8A, Shimadzu Co., Japan) equipped with an MS-5A column and a thermal conductivity detector (TCD).

The apparent quantum efficiency (AQE) was measured and calculated according to the following Eq. (1) [24,25]:

$$AQE = \frac{\text{Numberofreactedelectrons}}{\text{Numberofincidentphotons}} \times 100\%$$

$$= \frac{\text{NumberofevolvedH}_2\text{molecules} \times 2}{\text{Numberofincidentphotons}} \times 100\% = \frac{M \times N_A \times 2}{(I \times A)/(E_g \times J)} \times 100\% \quad (1)$$

In which, M is the average rate of H_2 evolution, N_A represents the Avogadro constant (6.02×10^{23}), I is the light intensity ($0.47\ mW\ cm^{-2}$), A is the aera of the incident light ($24.6\ cm^{-2}$), $E_g \times J$ is the energy of one 365 nm photon ($E_g = 1240/365$ nm, $J = 1.6 \times 10^{-19}$ j). The number of incident photons can be calculated to be 2.13×10^{19} photons s^{-1}.

2.8. Photoelectrochemical measurements

The ink solution for preparing working electrodes were prepared by dispersing 7.5 mg of photocatalysts into a mixture solution containing 375 μL of deionized water, 125 μL of ethanol and 30 μL of nafion and sonication for 30 min at room temperature. Then 30 μL of slurry was coated onto a fluorine-doped tin oxide glass (FTO, 1 cm^2) electrode by the doctor blade method. Next, the resulting electrodes were used by air drying and heated at 300 °C for 30 min in N_2 atmosphere. The electrochemical analysis was carried out using Bio-Logic VSP multichannel potentiostatic-galvanostatic system and a standard three-electrode cell was used. The prepared sample films working electrodes, an Ag/AgCl (saturated KCl) reference electrode, and a platinum plate counter electrode were also applied. The photocurrents were taken at an applied potential of 0 V *vs.* Ag/AgCl under simulated solar light irradiation provided by a 300 W Xe lamp in 0.35 M Na_2S/0.25 M Na_2SO_3 aqueous solution. The electrochemical impedance spectroscopy (EIS) measurements were performed in dark and under simulated solar light irradiation by applying an AC voltage with 5 mV amplitude in a frequency range from 0.01 Hz to 100 kHz under open circuit potential conditions in 0.35 M Na_2S/0.25 M Na_2SO_3 aqueous solution.

3. Results and discussion

3.1. ICP analysis

In order to study whether the target photocatalysts have been synthesized, the ICP analysis based on samples of ZCS and $Ni_{0.8}Co_{0.2}$/ZCS had been conducted, as shown in Table 1. As a result, we confirm that the obtained materials are the ones which we designed.

3.2. Ultrahigh photocatalytic H_2 evolution activities

The photocatalytic H_2 evolution activity was evaluated using an online gas chromatograph, and Fig. 1A shows the photograph evolution of H_2 bubbles on representative sample of $Ni_{0.8}Co_{0.2}$/ZCS in aqueous solution of 0.35 M Na_2S/0.25 M Na_2SO_3 + 5 mL triethanolamine (TEOA) under simulated solar light irradiation. Fig. 1B shows a comparison of photocatalytic H_2 evolution activities of ZCS and Ni_xCo_{1-x}/ZCS ($x = 0$, 0.5, 0.6, 0.8 and 1) in aqueous solutions containing 0.35 M Na_2S/0.25 M Na_2SO_3 and 5 mL of TEOA as hole scavengers under simulated solar light irradiation. ZCS NPs alone show high activity in photocatalytic H_2 evolution (70.0 mmol h^{-1} g^{-1}) because of the heterojunction constructed between CdS and ZnS, promoting the separation of photo-generated electron-hole pairs [26,27]. And yet, both pure CdS and ZnS show lower photocatalytic H_2 evolution rate of 14.8 and 20.1 mmol h^{-1} g^{-1} (Fig. 1C). It is clear that when Co or Ni as cocatalysts is being introduced, the H_2 evolution activities become to be enhanced. In addition, the much more superior activity is observed after introducing of the Ni_xCo_{1-x} and a maximum value of 211.4 mmol h^{-1} g^{-1} is reached, approximately 14, 11 and 3 times higher that of pristine CdS, ZnS, and ZCS, respectively. And the optimized molar ratio of Ni/Co is 0.8:0.2, which is probably due to the quite good "synergistic effect" between elements of Ni and Co [23]. Furthermore, $Ni_{0.8}Co_{0.2}$/ZCS shows much better activity than $Ni_{0.8}Co_{0.2}$/ZnS (Fig. S1), implying that heterojunction is exist in ZCS. As shown in Fig. 1D, $Ni_{0.8}Co_{0.2}$/ZCS demonstrates a much higher activity than Pt/ZCS (1%), meaning that $Ni_{0.8}Co_{0.2}$ bimetallic NPs can act as a quite better cocatalyst than Pt for ZCS. Fig. 1E shows the H_2 evolution rates of $Ni_{0.8}Co_{0.2}$/ZCS sample under both simulated solar and visible light ($\lambda > 420$ nm) irradiation, and these results clearly demonstrate that a high H_2 evolution rate (84.7 mmol h^{-1} g^{-1}) is achieved over $Ni_{0.8}Co_{0.2}$/ZCS even under visible light irradiation. Importantly, a high AQE value of 13.3% is obtained on the optimized photocatalysts of Ni_xCo_{1-x}/$Zn_{0.75}Cd_{0.25}S$ nanohybrids (Fig. S2).

For comparison, the photocatalytic H_2 evolution reactions over $Ni_{0.8}Co_{0.2}$/ZCS are successfully performed by using different hole scavengers (pure water, ethylene diamine tetraacetic acid (EDTA), TEOA, Na_2S/Na_2SO_3, Na_2S/Na_2SO_3 + EDTA, and Na_2S/Na_2SO_3 + TEOA) under identical conditions (Fig. 1F). Notably, $Ni_{0.8}Co_{0.2}$/ZCS exhibits superior H_2 evolution in an aqueous sacrificial solution containing 0.35 M Na_2S/0.25 M Na_2SO_3 and 5 mL of TEOA in comparison to any other sacrificial solutions. The above phenomena can be assigned to the reaction environment, where the transfer of photo-generated holes to the sacrificial donor can be accelerated in a relatively high alkaline solution [28]. In addition, the excellent performance for $Ni_{0.8}Co_{0.2}$/ZCS is much more clearly displayed in Fig. 1G. The recycling tests of the optimized photocatalyst are performed to evaluate the photocatalytic stability and the results are shown in Fig. S3. A little decreased photocatalytic H_2 evolution activity is observed after five cycling irradiation of 20 h, indicating the stability of $Ni_{0.8}Co_{0.2}$/ZCS for H_2 evolution. X-ray diffraction (XRD) patterns and X-ray photoelectron spectroscopy (XPS) analysis of the samples before and after the recycling experiment (Figs. S4, S5) also illustrates the exceeding stability of our photocatalysts. In summary, the significantly enhanced H_2 evolution and stability for $Ni_{0.8}Co_{0.2}$/ZCS can be attributed to the efficient charge separation and surface reactions. Our results show that it is a considerable evolution value on other kinds of semiconductor-based photocatalysts, and the comparison with already reported promising photocatalysts is shown in Table S1.

3.3. Structure and characterization

The powder XRD patterns and the typical scanning electron microscopy (SEM), transmission electron microscopy (TEM) and high-resolution TEM (HRTEM) are used to investigate the phase structures, morphology and composition of $Ni_{0.8}Co_{0.2}$/ZCS product. As shown in Fig. 2A, the CdS and ZnS species have hexagonal wurtzite and sphalerite phases with good crystallinity in accordance with JCPDS No. 41-1049 and 05-0566, respectively. Note that the XRD pattern of ZCS is different from that of either ZnS or CdS, another two weak signals are discovered in ZCS as compared with ZnS, indicating that the ZCS sample is not a mixture of CdS and ZnS (Figs. 2A, S6). In addition, the XRD pattern of ZCS shifts slightly to lower value compared with standard ZnS (Fig. S6B). The above results can be explained by the formation of $Zn_{0.75}Cd_{0.25}S$ solid solution [11,13]. In our case, the XRD pattern of NiCo NPs shows their metallic state (Fig. S7). However, for all the composites, no characteristic diffraction peaks of Ni_xCo_{1-x} (Figs. 2B, S6) can be found on account of their low amount, low crystallinity and high dispersion [29].

As shown in Fig. S8, the samples of ZCS and $Ni_{0.8}Co_{0.2}$/ZCS exhibit the morphologies of NPs with no obvious difference. SEM and TEM images of pure $Ni_{0.8}Co_{0.2}$ show that it is well-defined three-dimensional (3D) nanoflowers formed by ultrathin nanosheets (Figs. S9, S10). In Figs. 2C, D, TEM images of $Ni_{0.8}Co_{0.2}$/ZCS product show the irregular nanoparticle morphology with average size of 30 nm in diameter, no other products about Ni_xCo_{1-x} can be find dues to their low amount. In addition, the yellow region in Fig. 2E is amplified and clearly showed in Fig. 2F, that $Ni_{0.8}Co_{0.2}$/ZCS is constituted by two components of ZnS and CdS, and these interactions lead to the formation of an intact interface between them. The HRTEM image (Fig. 2F) shows that CdS has

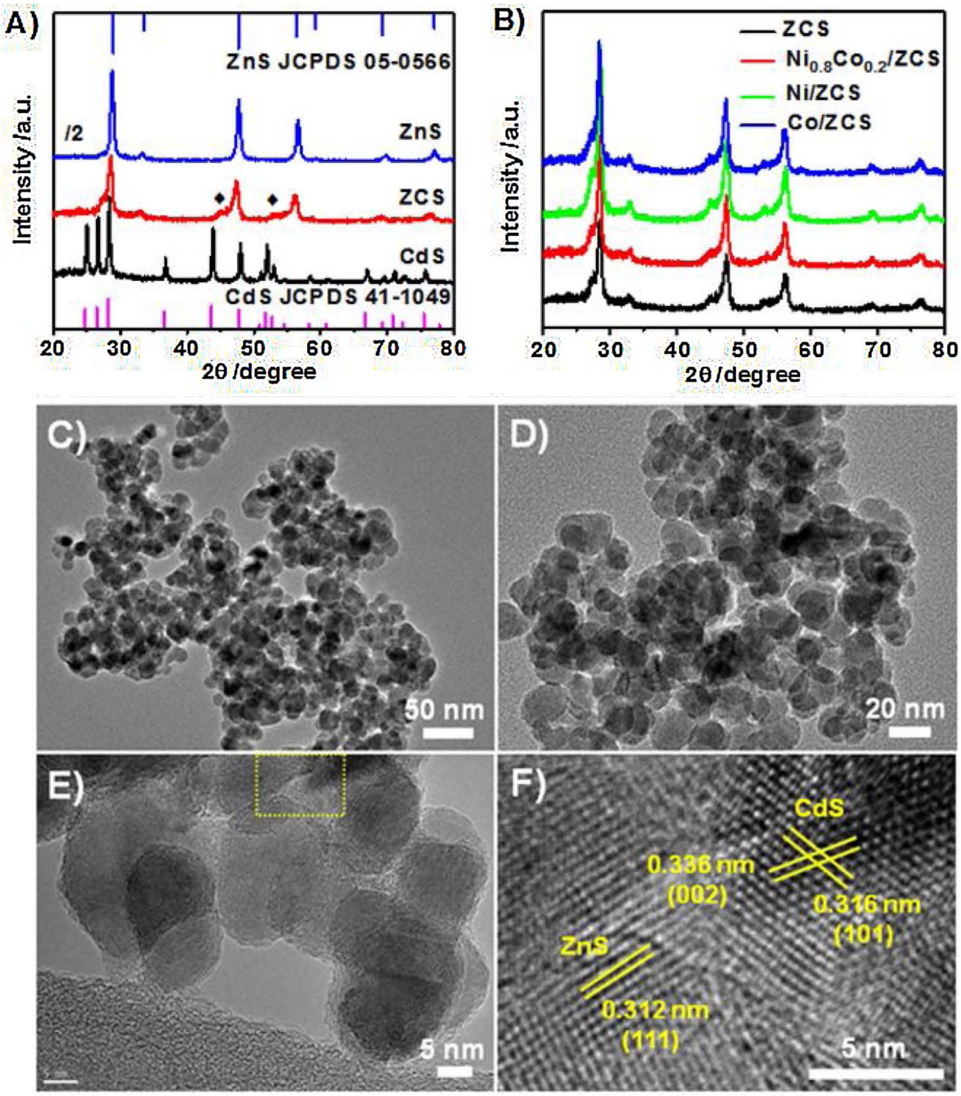

Fig. 2. XRD patterns of A) CdS, ZnS, and ZCS, and B) ZCS, $Ni_{0.8}Co_{0.2}$/ZCS, Ni/ZCS and Co/ZCS. TEM (C, D) and HRTEM (E, F) images of $Ni_{0.8}Co_{0.2}$/ZCS sample.

the lattice fringes with interplane spacing of 0.316 and 0.336 nm, corresponding to its (101) and (002) planes, while the 0.312 nm lattice fringe corresponded to the reflection from the (111) plane of ZnS. To further demonstrate the uniformly distribution of Ni and Co elements on the surface of Ni_xCo_{1-x}/ZCS hybrids, the energy-dispersive X-ray (EDX) spectroscopy and the elemental mapping images of Ni, Co, Zn, Cd, and S are analyzed and given in Figs. S11, S12. These results together with the following XPS analysis (Fig. 3) confirmed the existence of NiCo in specimen of Ni_xCo_{1-x}/ZCS.

To further verify the chemical composition and identify the chemical status of Ni_xCo_{1-x} in the prepared samples, XPS analysis is carried out. The full XPS survey spectrum of the $Ni_{0.8}Co_{0.2}$/ZCS is shown in Fig. 3A, demonstrating the main elements of Zn, Cd, S and C, and the trace of Ni and Co for their very low loading. The high-resolution XPS spectrum of Zn in the 2p region (Fig. 3B) shows two strong peaks at banding energies (BEs) of 1022.7 and 1045.7 eV, which can be assigned to Zn $2p_{3/2}$ and Zn $2p_{1/2}$, respectively, confirming a normal state of Zn^{2+} [30]. Fig. 3C shows the high-resolution XPS spectrum of Cd 3d, two signals located at 405.4 and 412.1 eV, which are in agreement with the BEs of Cd $3d_{5/2}$ and Cd $3d_{3/2}$, respectively, implying the state of Cd^{2+} in CdS [31,32]. In addition, the S 2p spectrum shows

one peak at 162.0 eV, which is attributed to S^{2-} in ZCS [30]. In order to confirm the positively effect and existence of Ni and Co, the XPS spectra of Ni 2p and Co 2p over $Ni_{0.8}Co_{0.2}$/ZCS are displayed in Fig. 3E, F. Clearly, as shown in Fig. 3E, two peaks located at 853.0 and 870.1 eV originate from the Ni $2p_{3/2}$ and Ni $2p_{1/2}$ species of metallic Ni are observed [33]. Meanwhile, the peak of Ni $2p_{3/2}$ at 854.8 eV is the divalent Ni^{2+} in NiO [11], and the peak of Ni $2p_{3/2}$ at 861.8 eV is the Ni^{2+} in Ni species [34], because of the fact that Ni element can be easily oxidized by O_2 in air and form a thin layer of NiO [35]. Furthermore, the XPS spectrum of Co 2p exhibits one unremarkable band at 794.1 eV, readily assigned to Co $2p_{1/2}$ of metallic Co [19]. However, two additional peaks at 783.6 and 799.2 eV are observed and can be ascribed to the higher oxidation states of cobalt [36], when metallic Co is exposed to the air. The above XPS observations together with the XRD result of NiCo NPs (Fig. S7) all confirms the fact that Ni and Co exist in metallic state.

3.4. Optical properties of Ni_xCo_{1-x}/ZCS

Fig. 4A shows a comparison of UV–vis diffuse reflectance spectra (UV–vis DRS) of ZCS, $Ni_{0.8}Co_{0.2}$/ZCS, Ni/ZCS and Co/ZCS. Pure ZCS shows the great enhancement of the absorption at about 510 nm for its corresponding band gap (E_g) of 2.44 eV by the Kubelka-Munk function (Fig. S13) [37–39] during to its intrinsic band-band transition. Compared with ZCS powder, the obtained $Ni_{0.8}Co_{0.2}$/ZCS and Co/ZCS show remarkably enhanced absorbance in the visible region ranging from 510 to 800 nm, especially to Co/ZCS. In addition, no shift of absorption edge was found after coupling with Ni, Co, or NiCo, implying that such metal specimen obtained by $NaBH_4$ reduction method are not

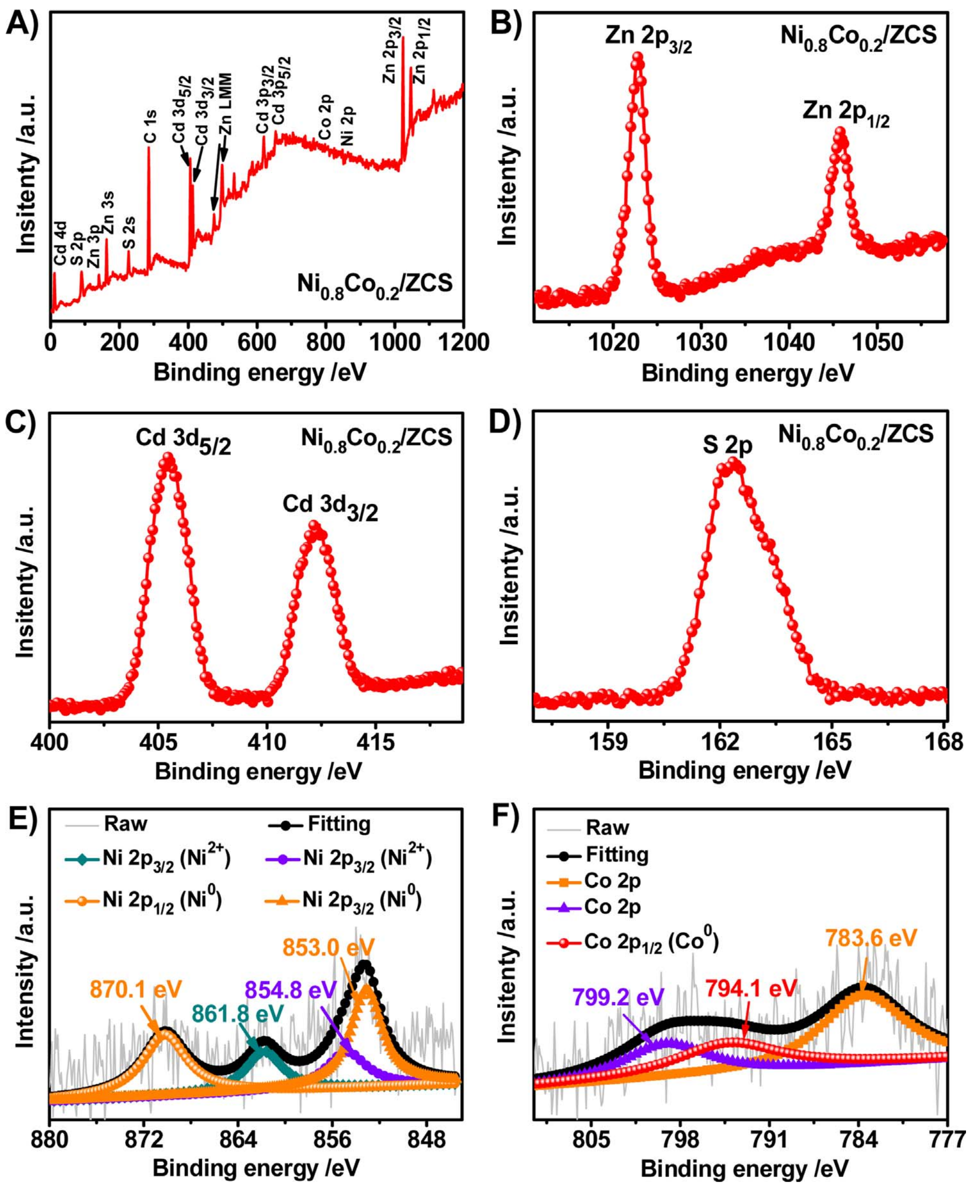

Fig. 3. XPS spectra of A) survey, B) Zn 2p, C) Cd 3d, D) S 2p, E) Ni 2p, and F) Co 2p for $Ni_{0.8}Co_{0.2}$/ZCS sample.

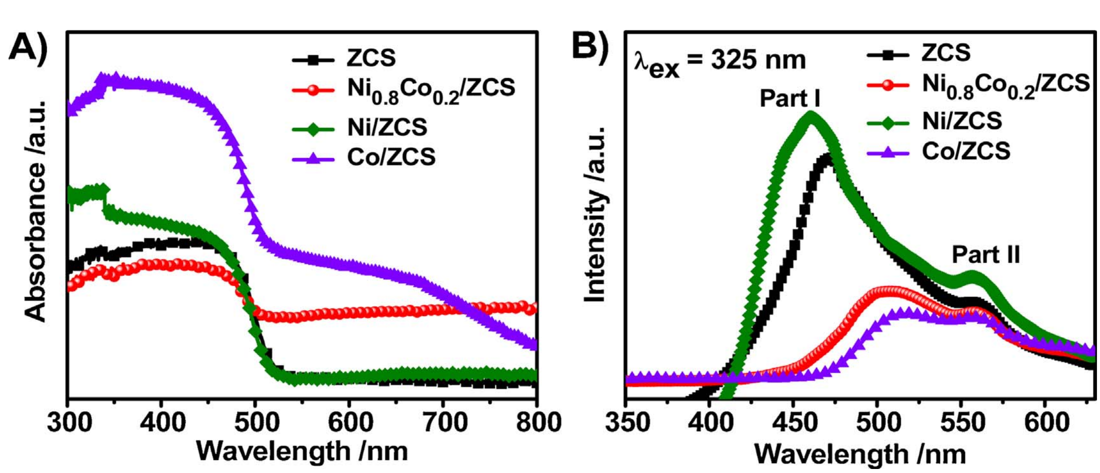

Fig. 4. A) UV–vis DRS spectra of ZCS, $Ni_{0.8}Co_{0.2}$/ZCS, Ni/ZCS and Co/ZCS samples. And B) PL emission spectra using 325 nm laser excitation for the as-prepared samples.

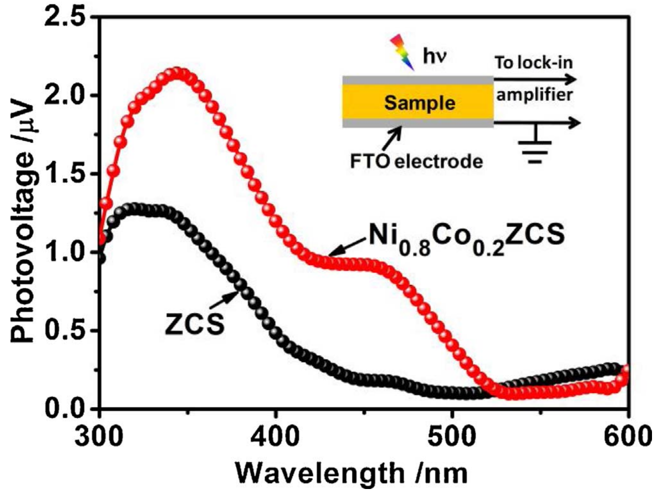

Fig. 5. SPV for ZCS and $Ni_{0.8}Co_{0.2}$/ZCS photocatalysts. Inset: a schematic setup for SPV measurement.

incorporated into the lattice of ZCS [11,29,40]. For comparison, the absorption spectra of Ni_xCo_{1-x}/ZCS (x = 0.5 and 0.8) is shown in Fig. S14.

To investigate the charge-carriers separation/recombination behaviors in Ni_xCo_{1-x}/ZCS system, the comparison photoluminescence (PL) emission spectra of ZCS, $Ni_{0.8}Co_{0.2}$/ZCS, Ni/ZCS and Co/ZCS excited at 325 nm are characterized in Figs. 4B, S15. The PL peaks of all Ni_xCo_{1-x}/ZCS products are dominated by two broad luminescence bands, that is, part I and part II. For an example of pure ZCS, part I and part II present the band to band optical emission peak and trap-state emission or surface defect state peak, respectively [41,42]. A drastic quenching of PL intensity for $Ni_{0.8}Co_{0.2}$/ZCS is found, indicating the recombination rate of the photo-generated electron-hole pairs is greatly suppressed [43,44]. The improved charge separation may be ascribed to the easy electron transfer from excited ZCS to NiCo, a synergistic effect between Ni and Co.

3.5. Enhanced photo-generated charge separation behaviors

The lock-in-based surface photovoltage (SPV) measurements are employed to investigete the photovoltaic properties of the obtained photocatalysts (Fig. 5). The response of pristine ZCS takes place in the range of 300–510 nm, which can be attributed to its intrinsic transition, indicating that the photo-generated charge carriers can achieve separation in space [45,46]. It is interesting to note that an obvious increased SPV response signal of $Ni_{0.8}Co_{0.2}$/ZCS is observed as compared to ZCS, illustrating its much strong charge separation efficiency [47]. Therefore, based on above fact, we speculate that the existence of interfacial electric field in $Ni_{0.8}Co_{0.2}$/ZCS composite plays the critical role in charge separation.

3.6. Photoelectrochemical properties

To provide an additional evidence for investigating the efficiency of the separation of photo-generated electron-hole pairs, a set of photoelectrochemical measurements are performed [5,48–51]. The comparison photocurrent transient response for ZCS and $Ni_{0.8}Co_{0.2}$/ZCS with typical on-off switches of intermittent under simulated solar irradiation at a bias potential of 0 V *vs*. Ag/AgCl in 0.35 M Na_2S/0.25 M Na_2SO_3 aqueous solution are shown in Fig. 6A. It is worth noting that the photocurrent response of $Ni_{0.8}Co_{0.2}$/ZCS is enhanced greatly compared with that of ZCS, suggesting that a distinct improvement in the separation of photo-generated electron-hole pairs can be achieved after loading of Ni_xCo_{1-x} [5].

Moreover, the transient decay time plots are also performed to study the lifetime of photo-generated charge carriers in the obtained two photoelectrodes in qualitative. Thus the transient decay times for pure ZCS and $Ni_{0.8}Co_{0.2}$/ZCS can be expressed by a logarithmic plot of the parameter D according to the following Eq. (2) [52,53]:

$$D= \frac{I_t - I_s}{I_0 - I_s} \tag{2}$$

where I_t is the photocurrent at time t, I_s is the photocurrent achieved once the charge evolution and recombination rates reach equilibrium, and I_0 is the photocurrent occurs immediately upon illumination. The transient decay time is named as the time at which ln D = –1 [52]. Notably, as shown in Fig. 6B, the $Ni_{0.8}Co_{0.2}$/ZCS material shows much longer transient decay time than that of pure ZCS, suggesting the longer charge carries lifetime for $Ni_{0.8}Co_{0.2}$/ZCS photoelectrode. The above results confirm that the behavior of photo-generated charge carriers play the key role in photocatalytic H_2 evolution under simulated solar light illustration.

Electrochemical impedance spectroscopy (EIS) Nyquist plots are a significative tool to characterize the charge carrier migration of the electrode materials, then the EIS Nyquist plots over ZCS and $Ni_{0.8}Co_{0.2}$/ZCS are measured at the open circuit potential both in dark and under light (Fig. 6C) [40,50,54]. Generally, the semicircle appears in the EIS Nyquist plots reflect the charge transfer resistance at the electrode interface [55]. The smaller semicircular arc of the EIS plot is, the higher transfer rate of interfacial charge transfer [40]. As a result, the introduction of Ni_xCo_{1-x} boosts the charge transfer rate at the electrode interface, resulting in an effective separation of photo-generated electron-hole pairs. Additionally, no decrease of photocurrent is observed for Ni_xCo_{1-x}/ZCS in the test of 3 h, suggesting its high stable activity (Fig. 6D).

3.7. Mechanism of Ni_xCo_{1-x}/ZCS exploration

It is important to clarify the underlying reason for significant improvement of the photocatalytic H_2 evolution performance on these modified ZCS samples. We then conducted work function (W_m and W_s for metal and semiconductor, respectively) measurements to illustrate the charge injection behaviors. Scheme 1A presents the work functions of Au, ZCS, NiCo, Ni, and Co samples, which is a product of ΔCPDs between the samples and the Au probe detected by using a Kelvin probe. The work functions are calculated using the following equation (3) [56]:

$$W_{sample} = W_{Au} + \Delta CPD/1000 \tag{3}$$

where W_{Au} is 5.1 eV. As a result, the work functions of ZCS, NiCo, Ni, and Co are 5.03, 4.89, 4.73, and 4.54 eV, respectively, as can be seen clearly in Scheme 1B.

Based on the E_g of ZCS (2.44 eV, Fig. S13), the energy of CB (E_{CB}) and valence band (E_{VB}) are obtained with the following Eqs (4–5) [57]:

$$E_{CB} = -W + 0.5\ E_g \tag{4}$$

$$E_{VB} = -W - 0.5\ E_g \tag{5}$$

As a result, the E_{CB} and E_{VB} for ZCS are calculated to be −0.69 and 1.75 eV versus normal hydrogen electrode (*vs*. NHE), respectively. In summary, the energy level positions of ZCS, NiCo, Ni, and Co samples are shown in Scheme 1C.

As can be seen in Scheme 2A, the band structure of $Zn_{0.75}Cd_{0.25}S$ formed by CdS and ZnS is clearly given. Under the simulated solar light irradiation, both CdS and ZnS can be motivated and generate electrons and holes. VB-holes of CdS can be transferred to the intrinsic defects positions of zinc vacancies (V_{Zn}) and interstitial sulfur vacancies (V_S) in ZnS [26,27], then CB-electrons of ZnS can be transferred to CB of CdS, which promotes efficient charge transfer in ZnCdS (CdS/ZnS hybrid) and resulting in a much higher photocatalytic H_2 evolution than both

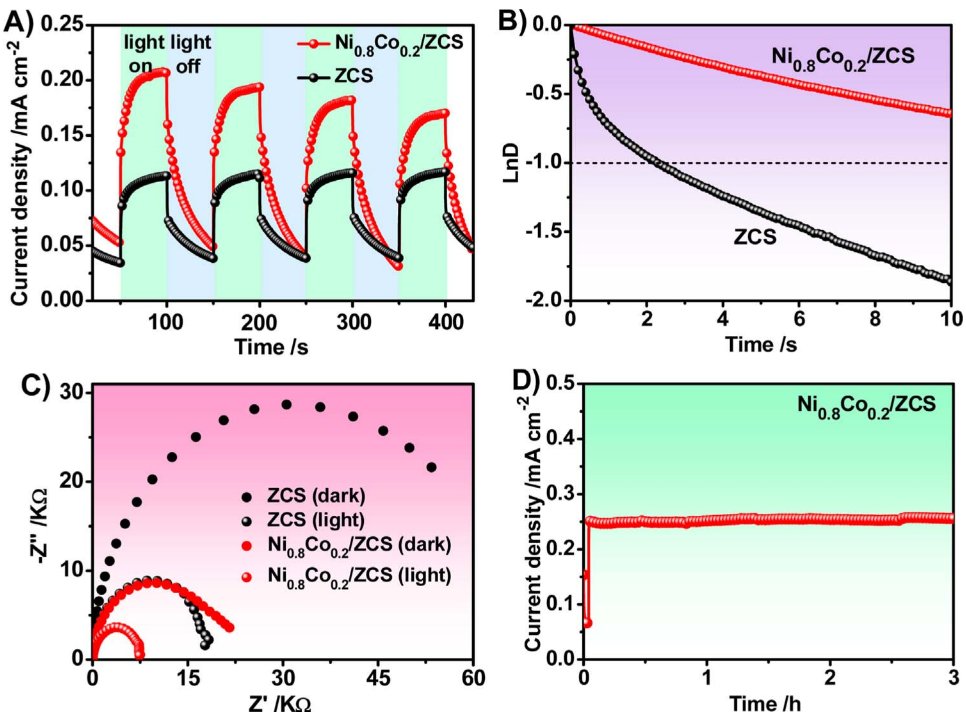

Fig. 6. A) Transient photocurrent density versus time for ZCS (the bottom curver) and Ni0.8Co0.2/ZCS (the top curver) under simulated solar light irradiation. B) Transient decay times for ZCS and $Ni_{0.8}Co_{0.2}$/ZCS hybrid. C) EIS Nyquist plots of ZCS and $Ni_{0.8}Co_{0.2}$/ZCS at the open circuit potential in the dark and under simulated solar light irradiation. D) Time-dependent *I-t* curves of $Ni_{0.8}Co_{0.2}$/ZCS at 0 V *vs.* Ag/AgCl.

that of pristine of CdS and ZnS (Fig. 1C). It is well known that a Schottky junction will be formed when a metal intimate contact with a semiconductor, because of their difference in work function, leading to the bend of the conduction band [58,59]. In this case, the work function of ZCS is larger than that of the Co, Ni or NiCo ($W_s > W_m$), electrons will transfer from Co, Ni or NiCo with the higher Fermi levels to ZCS with the lower one, thus the downward band bending is formed until the Fermi levels for both phases are equal [58]. As a result, the separation and transfer of photo-generated electrons and holes can be quickened under the function of band bending, thus metal surface will being the accumulated electrons and semiconductor surface the accumulated holes participating in reduction and oxidation reactions, respectively [58]. Obviously, after metal and semiconductor come contact, the equilibrium state of the Fermi level is between the E_{fs} and E_{fm}, and the CB for ZCS shifts accordingly higher energy level. The change value of the E_{CB} for ZCS can be reckoned as the half of the difference of the work functions between Co and ZCS, for example, that is 0.25 eV. Then the E_{CB} and E_{VB} for ZCS after modification of Co are −0.94 and

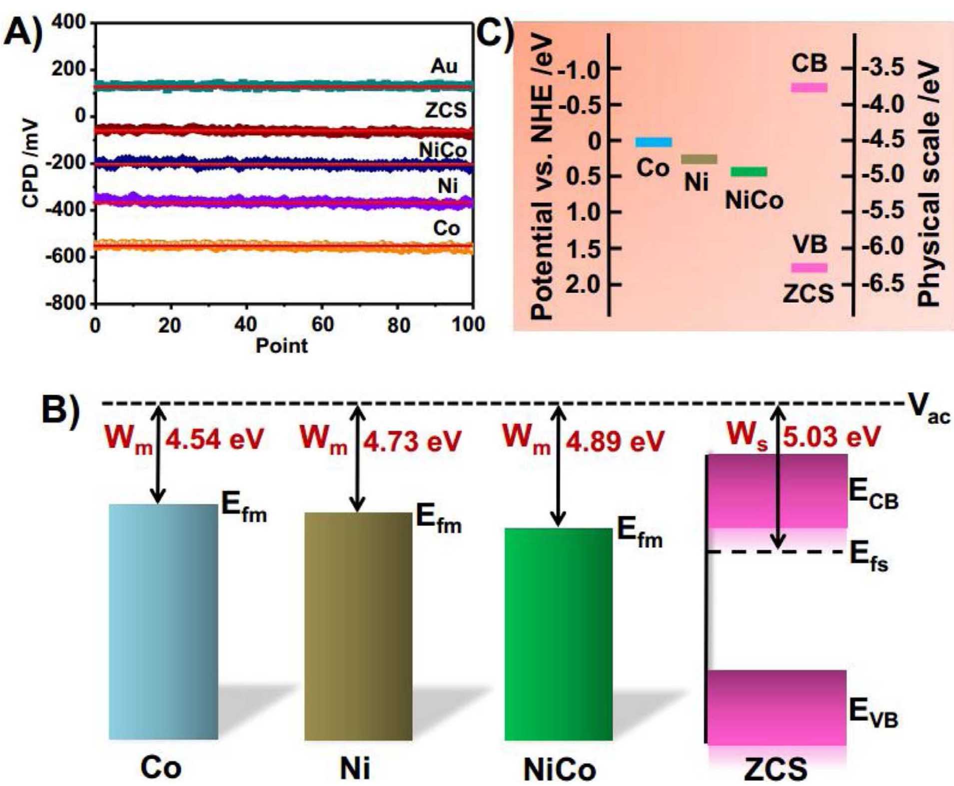

Scheme 1. A) The work functions, B) the schematic diagram of the work functions, V_{ac} is the vacuum level, E_{fm} and E_{fs} are the Fermi level of metal and semiconductor, and C) the energy level positions of ZCS, NiCo, Ni, and Co samples.

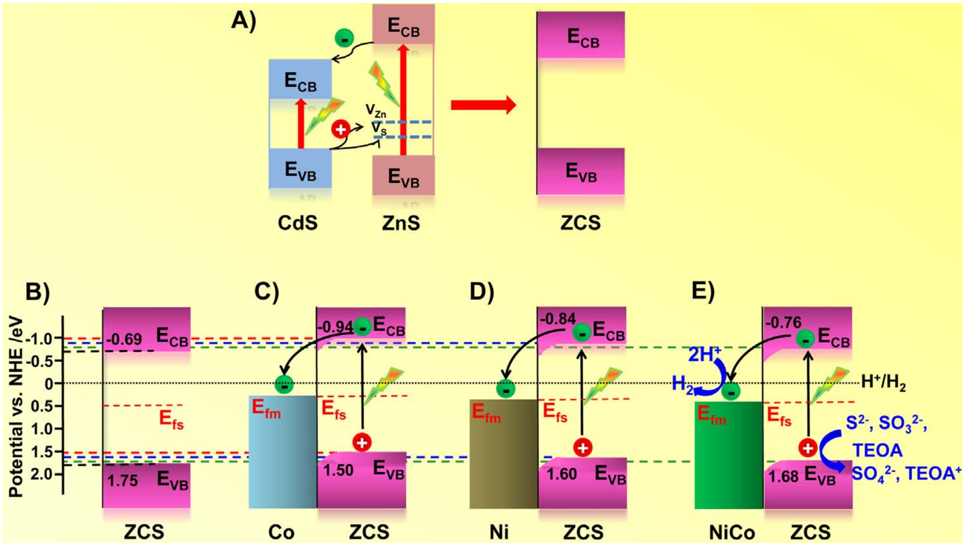

Scheme 2. Schematic band illustrations of A) band structure alignments of the CdS/ZnS (ZCS) product, B) Co/ZCS, C) Ni/ZCS, and D) NiCo/ZCS and the charge transfer driven by the Schottky junction in the hybrid structures under simulated light irradiation in 0.35 M Na_2S/0.25 M $NaSO_3$ + TEOA aqueous solution.

1.50 eV *vs.* NHE, respectively. Similary, the E_{CB} and E_{VB} for ZCS after contaction with Ni or NiCo are also reckoned and illustrated in Scheme 2.

From above analysis, we can see that the formed equilibrium Fermi energy potential of Ni/ZCS is lower than that of Co/ZCS (as shown in Scheme 1C and D), indicating that the transfer driving force to boost the efficient separation and transfer of photo-generated electrons between Ni and ZCS is much higher in comparison with Co and ZCS, which is quite consistent with the results of photocatalytic H_2 evolution from water splitting (Fig. 1). For Ni_xCo_{1-x} alloys, the much larger W_m than both that of Ni and Co results in its much lower Fermi energy level, suggesting that one " synergistic effect" between Ni and Co may be exist. Thus, in the Ni_xCo_{1-x}/ZCS hybrid, the above result makes the photo-generated electrons much more beneficial to accumulate on the alloys, meaning that the charge capture ability is improved [23,60]. As a result, the CB-electrons of ZCS prefer to as well as quickly transfer to Ni_xCo_{1-x} NPs to participate the H_2 evolution reaction, results in much higher photocatalytic activity.

Under solar light irradiation, ZCS can be easily activated and generates electrons and holes staying in the CB and VB, respectively. Then, CB-electrons of ZCS transfer to the Ni_xCo_{1-x} alloy under the function of Schottky barrier and accumulate on the Ni_xCo_{1-x} NPs reduction active sites for participating H_2 evolution reaction. The VB-holes of ZCS are scavenged by scavengers of TEOA, S^{2-}/SO_3^{2-} to oxidize $TEOA^+$ and SO_4^{2-}. In this way, the good separation and transfer of photo-generated electron-hole pairs lead to the remarkable enhancement of photocatalytic H_2 evolution in the Ni_xCo_{1-x}/ZCS nanohybrid. Significantly, the work present here provides a new concept to design and prepare such novel non-noble-metal based nanoparticle cocatalyst materials with ultrahigh activities for applications in solar energy conversion and utilization.

4. Conclusion

In summary, in this paper we first developed a novel Ni_xCo_{1-x}/ZCS nanohybrid photocatalyst by regulating the transfer behavior of photo-generated charge carriers and achieving such an impressive photocatalytic H_2 evolution rate of 211.4 mmol h^{-1} g^{-1} under solar light irradiation. This is one of the most promising photocatalysts as we know. It is demonstrated that the Ni_xCo_{1-x} NPs has an optimal charge-transfer-capture ability towards H^+ reduction. The research presented here has profound advantages for its low cost, facile synthesis. We believe that Ni_xCo_{1-x} alloy can be the most promising candidates in photocatalytic reaction.

Acknowledgements

This work was financially supported by the National Natural Science Foundation of China (Nos. 20841003, 21261130584, 21390394, 91022030, 20971052, and 20741001), the Chang Bai Mountain Scholars Program (440020031182) and the Graduate Innovation Fund of Jilin University.

Appendix A. Supplementary data

Supplementary data associated with this article can be found, in the online version, at http://dx.doi.org/10.1016/j.apcatb.2017.10.010.

References

[1] X.C. Wang, K. Maeda, A. Thomas, K. Takanabe, G. Xin, J.M. Carlsson, K. Domen, M. Antonietti, Nat. Mater. 8 (2009) 76–80.
[2] J.H. Yang, D.G. Wang, H.X. Han, C. Li, Acc. Chem. Res. 46 (2013) 1900–1909.
[3] X.B. Chen, S.H. Shen, L.J. Guo, S.S. Mao, Chem. Rev. 110 (2010) 6503–6570.
[4] S. Balasubramanian, P. Wang, R.D. Schaller, T. Rajh, E. Rozhkova, Nano Lett. 13 (2013) 3365–3371.
[5] K. Chang, Z.W. Mei, T. Wang, Q. Kang, S.X. Ouyang, J.H. Ye, ACS Nano 8 (2014) 7078–7087.
[6] K. Maeda, M. Eguchi, T. Oshima, Angew. Chem. Int. Ed. 53 (2014) 13164–13168.
[7] Y. Xia, Q. Li, K. Lv, D. Tang, M. Li, Appl. Catal. B: Environ. 206 (2017) 344–352.
[8] L. Mu, Y. Zhao, A. Li, S. Wang, Z. Wang, J. Yang, Y. Wang, T. Liu, R. Chen, J. Zhu, Energy Environ. Sci. 9 (2016) 2463–2469.
[9] K. Maeda, M. Higashi, D.L. Lu, R. Abe, K. Domen, J. Am. Chem. Soc. 132 (2010) 5858–5868.
[10] B. Qiu, Q. Zhu, M. Du, L. Fan, M. Xing, J. Zhang, Angew. Chem. Int. Ed. 56 (2017) 2684–2688.
[11] J.R. Ran, J. Zhang, J.G. Yu, S.Z. Qiao, ChemSusChem 7 (2014) 3426–3434.
[12] N. Kakuta, K. Park, M. Finlayson, A. Ueno, A. Bard, A. Campion, M. Fox, S. Webber, J. d. White, J. Phys. Chem. 89 (1985) 732–734.
[13] J. Zhang, Q.L. Xu, S.Z. Qiao, J.G. Yu, ChemSusChem (2013) 2009–2015.
[14] B. Qiu, Q. Zhu, M. Xing, J. Zhang, Chem. Commun. 53 (2017) 897–900.
[15] H. Du, X. Xie, Q. Zhu, L. Lin, Y.F. Jiang, Z.K. Yang, X. Zhou, A.W. Xu, Nanoscale 7 (2015) 5752–5759.
[16] M. Nguyen, P.D. Tran, S.S. Pramana, R.L. Lee, S.K. Batabyal, N. Mathews, L.H. Wong, M. Graetzel, Nanoscale 5 (2013) 1479–1482.
[17] J. Zhang, J.G. Yu, M. Jaroniec, J.R. Gong, Nano Lett. 12 (2012) 4584–4589.
[18] X.Z. Yue, S.S. Yi, R.W. Wang, Z.T. Zhang, S.L. Qiu, Sci. Rep. 6 (2015) 22268–22276.
[19] P.D. Tran, L.F. Xi, S.K. Batabyal, L.H. Wong, J. James Barber, J.S.L. Loo, Phys. Chem. Chem. Phys. 14 (2012) 11596–11599.
[20] K.W. Nam, J. Song, K.H. Oh, M.J. Choo, H. Park, J.K. Park, J.W. Choi, Carbon 50 (2012) 3739–3747.
[21] Z.B. Jiao, Y. Zhang, S.X. Ouyang, H.C. Yu, G.X. Lu, J.H. Ye, Y.P. Bi, ACS Appl. Mater. Interfaces 6 (2014) 19488–19493.
[22] J.Q. Tian, N.Y. Cheng, Q. Liu, X.P. Sun, Y.Q. He, A.M. Asiri, J. Mater. Chem. A 3 (2015) 20056–20059.
[23] C.C. Han, Y. Lu, J.L. Zhang, L. Ge, Y.J. Li, C.F. Chen, Y.J. Xin, L.E. Wu, S.M. Fang, J. Mater. Chem. A 3 (2015) 23274–23282.
[24] S. Xiao, P. Liu, W. Zhu, G. Li, D. Zhang, H. Li, Nano Lett. 15 (2015) 4853–4858.

[25] K. Chang, M. Li, T. Wang, S.X. Ouyang, P. Li, L.Q. Liu, J.H. Ye, Adv. Energy Mater. 5 (2015) 1402279–1402288.
[26] Y.P. Xie, Z.B. Yu, G. Liu, X.L. Ma, H.M. Cheng, Energy Environ. Sci. 7 (2014) 1895–1901.
[27] D.C. Jiang, Z.J. Sun, H.X. Jia, D.P. Lu, P.W. Du, J. Mater. Chem. A 4 (2016) 675–683.
[28] P. Wu, J. Wang, J. Zhao, L. Guo, F.E. Osterloh, Chem. Commun. 50 (2014) 15521–15524.
[29] J. Zhang, L.F. Qi, J.R. Ran, J.G. Yu, S.Z. Qiao, Adv. Energy Mater. 4 (2014) 1301925–1301930.
[30] R.S. Zeng, Z.G. Sun, S. Cao, R.G. Shen, Z.J. Liu, Y. Xiong, J.T. Long, J.J. Zheng, Y.Q. Zhao, Y.Y. Shen, D.S. Wang, RSC Adv. 5 (2015) 1083–1090.
[31] S.N. Guo, Y.L. Min, J.C. Fan, Q.J. Xu, ACS Appl. Mater. Interfaces 8 (2015) 2928–2934.
[32] B. Chai, T.Y. Peng, P. Zeng, X.H. Zhang, Dalton Trans. 41 (2012) 1179–1186.
[33] L.L. Bi, D.D. Xu, L.J. Zhang, Y.H. Lin, D.J. Wang, T.F. Xie, Phys. Chem. Chem. Phys. 17 (2015) 29899–29905.
[34] X.X. Zou, J. Su, R. Silva, A. Goswami, B.R. Sathe, T. Asefa, Chem. Commun. 49 (2013) 7522–7524.
[35] A.K. Agegnehu, C.J. Pan, J. Rick, J.F. Lee, W.N. Su, B.J. Hwang, J. Mater. Chem. 22 (2012) 13849–13854.
[36] O. Metin, S. Ozkar, Energ. Fuel. 23 (2009) 3517–3526.
[37] Q.J. Guo, H.W. Hillhouse, R.J. Agrawal, J. Am. Chem. Soc. 131 (2009) 11672–11673.
[38] S. Sakthivel, H. Kisch, Angew. Chem. Int. Ed. 42 (2003) 4908–4911.
[39] F. Gao, X.Y. Chen, K.B. Yin, S. Dong, Z.F. Ren, F. Yuan, T. Yu, Z. Zou, J.M. Liu, Adv. Mater. 19 (2007) 2889–2892.
[40] Q. Li, H. Meng, J.G. Yu, W. Xiao, Y.Q. Zheng, J. Wang, Chem-Eur J. 20 (2014) 1176–1185.
[41] T.Y. Zhai, Z.J. Gu, W.S. Yang, X.Z. Zhang, J. Huang, Y.S. Zhao, D.P. Yu, H.B. Fu, Y. Ma, J.N. Yao, Nanotechnology 17 (2006) 4644–4649.
[42] X. Zhong, S. Liu, Z. Zhang, L. Li, Z. Wei, W. Knoll, J. Mater. Chem. 14 (2004) 2790–2794.
[43] G.G. Zhang, M.W. Zhang, X.X. Ye, X.Q. Qiu, S. Lin, X.C. Wang, Adv. Mater. 26 (2014) 805–809.
[44] J.S. Zhang, M.W. Zhang, C. Yang, X.C. Wang, Adv. Mater. 26 (2014) 4121–4126.
[45] I. Mora-Sero, T. Dittrich, A. Belaidi, G. Garcia-Belmonte, J. Bisquert, J. Phys. Chem. B 109 (2005) 14932–14938.
[46] D.D. Xu, T.F. Jiang, D.J. Wang, L.P. Chen, L.J. Zhang, Z.W. Fu, L.L. Wang, T.F. Xie, ACS Appl. Mater. Interfaces 6 (2014) 9321–9327.
[47] Z. Liu, D.D. Sun, P. Guo, J.O. Leckie, Nano Lett. 7 (2007) 1081–1085.
[48] Y.H. Zhang, Z.R. Tang, X. Fu, Y.J. Xu, ACS Nano 5 (2011) 7426–7435.
[49] Z.H. Zhang, L.B. Zhang, M.N. Hedhili, H.N. Zhang, P. Wang, Nano Lett. 13 (2013) 14–20.
[50] Q.J. Xiang, J.G. Yu, M. Jaroniec, J. Am. Chem. Soc. 134 (2012) 6575–6578.
[51] N. Zhang, M.Q. Yang, Z.R. Tang, Y.J. Xu, ACS Nano 8 (2014) 623–633.
[52] N.J. Bell, Y.H. Ng, A. Du, H. Coster, S.C. Smith, R.J. Amal, Phys. Chem. C 115 (2011) 6004–6009.
[53] L. Zhang, E. Reisner, J.J. Baumberg, Energy Environ. Sci. 7 (2014) 1402–1408.
[54] H.L. Guo, X.F. Wang, Q.Y. Qian, F.B. Wang, X.H. Xia, ACS Nano 3 (2009) 2653–2659.
[55] X. Yu, J. Zhang, Z. Zhao, W. Guo, J. Qiu, X. Mou, A. Li, J.P. Claverie, H. Liu, Nano Energy 16 (2015) 207–217.
[56] S. Li, L.B. Hou, L.J. Zhang, L.P. Chen, Y.H. Lin, D.J. Wang, T. Xie, J. Mater. Chem. A 3 (2015) 17820–17826.
[57] F. Ning, M. Shao, S. Xu, Y. Fu, R. Zhang, M. Wei, D.G. Evans, X. Duan, Energy Environ. Sci. 9 (2016) 2633–2643.
[58] S. Bai, J. Jiang, Q. Zhang, Y.J. Xiong, Chem. Soc. Rev. 44 (2015) 2893–2939.
[59] H.B. Michaelson, J Appl. Phys. 48 (1977) 4729–4733.
[60] Z. Hu, J.C. Yu, J. Mater. Chem. A 1 (2013) 12221–12228.